https://doi.org/10.3311/PPtr.40053

Periodica Polytechnica Transportation Engineering

Design and Dynamic Modeling of Magnetorheological Elastomer Battery Pack Dampers for Electric Vehicles

Ahmad Robiul Awal Udin[1,2], Harus Laksana Guntur[1*], Ubaidillah Ubaidillah[3], Seung-Bok Choi[4], Fahmi Mubarok[1]

[1] Departement of Mechanical Engineering, Institut Teknologi Sepuluh Nopember, Building C, Teknik Industri Street, Sukolilo Campus, 60111 Surabaya, East Java, Indonesia
[2] Automotive Engineering Department, Politeknik Negeri Jember, Mastrip Street P.O. Box 164, 68101 Jember, East Java, Indonesia
[3] Mechanical Engineering Department, Faculty of Engineering, Universitas Sebelas Maret, Ir. Sutami Street 36A, 57126 Surakarta, Central Java, Indonesia
[4] Department of Mechanical Engineering, The State University of New York- SUNY, Korea, 119 Songdo Moonhwa-Ro, Yeonsu-Gu, 21985 Incheon, South Korea
* Corresponding author, e-mail: haruslg@me.its.ac.id

Received: 01 February 2025, Accepted: 15 December 2025, Published online: 23 April 2026

Abstract

Electric vehicle battery packs and other components are vulnerable to vibration excitation caused by external variables like road profile because of their unique properties and dynamic reactivity. The application of passive, semi active, and active vibration isolation methods in suspension systems, drive engines, and other vehicle components presents both advantages and disadvantages. This study examines the optimization of battery pack damper parameters using magnetorheological elastomer (MRBD) material, employing a genetic algorithm (GA) technique with magnetic fields produced by 1A and 2A electric currents integrated into electric vehicle pack batteries. 1A and 2A MRBD battery pack dampers have a lower peak transmissibility amplitude than without dampers (WOMRBD), according to simulation results of the dynamic response with input parameters of vehicle speed variations of 10, 20, and 30 km/h. In particular, there is a significant decrease in the peak MRBD 2A, which is more optimal at 0.086 at a medium frequency of 13.4 Hz. Additionally, the power dissipated by MRBD 1A and 2A while absorbing vibrational energy is sent to the battery pack at efficiencies of 51.4% and 39.3%, respectively, in contrast to the scenario without a damper (WOMRBD), specifically at a velocity of 20 km/h.

Keywords

damper, battery pack, magnetorheological elastomer, electric vehicle, dynamic response

1 Introduction

One of the most demanding components of Electric Vehicle's (EVs) that is vulnerable to changes in the mechanical characteristics and vibration excitation is the battery pack (Heinzen et al., 2023). The battery pack contains an array of modules and battery cells as the main source of drive (power train source) in electric vehicles (Hua and Thomas, 2021). The battery packs are designed to withstand thermal, impact, and vibration loads (Shui et al., 2018). Dynamic loading and random vibrations from uneven or sinusoidal road surfaces can affect the safety and reliability of the battery pack and the electrical system of the battery pack of MPEV-type electric vehicles at certain speeds, which require the design of vibration isolators or battery pack mounting. Vibration excitation changes are affected by a range of factors in all environmental settings, such as road topography (Hári, 2022). This vibration condition is problematic when the vehicle is in motion at a specific speed, not only compromising comfort but also posing a risk to the longevity of vehicle components (Székely and Ficzere, 2017). Vibration changes have time and impact characteristics that affect material strength (Abdillah et al., 2021). The SAE J2380 standard excitation frequency for the vibration testing of electric vehicle battery packs is 10-190 Hz whose amplitude excitation profile is adjusted to the road profile (SAE International Recommended Practice, 2013). If the excitation frequency exceeds the natural frequency of the battery pack, the vibration response does not contribute to each vibration mode. Therefore, the PSD magnitude is influenced by the amplitude in the excitation frequency range (Yang et al., 2022).

Cite this article as: Udin, A. R. A., Guntur, H. L., Ubaidillah, U., Choi, S.-B., Mubarok, F. (2026) "Design and Dynamic Modeling of Magnetorheological Elastomer Battery Pack Dampers for Electric Vehicles", Periodica Polytechnica Transportation Engineering, https://doi.org/10.3311/PPtr.40053

The dynamic modeling of a quarter-DOF electric vehicle moving at a certain speed on an uneven or sinusoidal road surface trajectory will provide information on the magnitude of the vibration response and working frequency (Zhao and Nagayama, 2017). The frequency response of a vehicle moving on an uneven or irregular road is 1–30 Hz (Prażnowski and Mamala, 2016). The frequency is a function of the wheel stiffness, spring (suspension) stiffness, and vehicle sprung mass stiffness (Nguyen et al., 2020; Yudianto et al., 2019). The frequency response parameters in the 5-DOF half-vehicle modeling for the front and rear wheels, front and rear suspension, and steering have different acceleration characteristics with respect to frequency due to the influence of the road profile (Susatio et al., 2018). The impact of frequency changes the transmissibility in half-vehicle modeling when using damper variations (Zhu et al., 2018).

The influence of the road profile (bump) on the transmissibility between the components of the vibration source can cause changes in the system frequency (Ramalingam et al., 2020). The damping systems in EVs include not only suspensions but also dampening electrical components, including batteries in battery cases that function to reduce the transmissibility of vibration sources in sprung mass components (Belingardi and Scattina, 2023). The application of a magnetorheological elastomer as an isolator or vibration damper has the advantage of flexible and responsive stiffness in a wide spectrum of excitation frequencies compared with passive damper isolators such as rubber (constant stiffness). The magnetorheological elastomer was composed of a polymer and carbonyl iron particles (CIP) with certain compositions. Polymeric materials are commonly used as magnetorheological elastomers (MRE) as a matrix of natural rubber, polyurethane, room temperature vulcanizing (RTV) silicone rubber, elastomer etc. (Liu et al., 2020; Priyandoko et al., 2021; Sobri et al., 2024). The spatial distribution and alignment of carbonyl iron particles (CIPs) within both isotropic and anisotropic elastomeric matrices can be strategically manipulated through the externally applied magnetic field, which is dynamically generated by the passage of an electric current, thereby enabling controlled modulation of the composite's microstructural configuration and potentially enhancing its magneto-responsive mechanical properties (Khairi et al., 2024). The optimization of the MRE parameters using a genetic algorithm (GA) was carried out to find parameters suitable for modeling and applying dampers to be more effective in projecting a decrease in transmissibility and increasing vibration absorption so that it is not transmitted to other component parts (Tang et al., 2023; Yu et al., 2019). The application of active or semi-active MRE dampers in engine mounting has a lower transmissibility force than passive mounting dampers (Ladipo et al., 2016; Zainordin and Mohamed, 2024). Based on the literature review above, this study evaluates and compares the simulation results of the electric vehicle dynamic models in terms of the dynamic response, damping force magnitude, and power density spectral distribution to establish a suitable working frequency range for the battery pack, thus preventing resonance with the system's natural frequency. The variations used include battery packs without (WOMRBD) and those using magnetorheological elastomer dampers (MRBD) that have been optimized using a genetic algorithm (GA) based on MRE parameters of previous research through the generation of 1 and 2A current magnetic fields with the designations MRBD 1A and MRBD 2A, respectively (Yu et al., 2019). The input simulation parameters include sinusoidal road profiles that serve as the excitation source for electric vehicles traveling at speeds of 10, 20, and 30 km/h, allowing for a comparison of half-vehicle dynamic modeling defined as 6 degrees of freedom (DOF) both with the semi-active magnetorheological elastomer battery pack damper (MRBD) and without it (the battery pack bolted to the vehicle chassis, referred to as WOMRBD).

2 Methodology

The research parameters included the determination of vehicle speed and road surface profile, which determined the magnitude of the excitation frequency according to the ISO 8606:2016 standard (Galvagno et al., 2018; ISO, 2016). Furthermore, a numerical modeling analysis was conducted to evaluate the magnitude of the battery pack's dynamic response with and without a magnetorheological damper.

2.1 Road profile

The excitation frequency in ISO 8606:2016 standard is equivalent to the temporal frequency of the vehicle while traveling at a certain speed (v) (ISO, 2016). The spatial frequency requirement of the off-road profile is above 0.05 cycles/m, which means that the road irregularity trajectory can extend as far as 20 m. Relationship between temporal frequency (f_t) and spatial frequency (n):

$$ft = n \cdot v \,. \tag{1}$$

The excitation frequency at vehicle speeds of 10, 20, and 30 km/h can be determined by using Eq. (1) (Abdillah et al., 2021). Fig. 1 shows a wavy track length of 2 m with a spatial frequency (n) of 0.5 cycles/m so that the temporal/excitation frequency (ω_{ext}) of each vehicle speed is 1.39, 2.78, and 4.17 Hz, respectively. The road profile

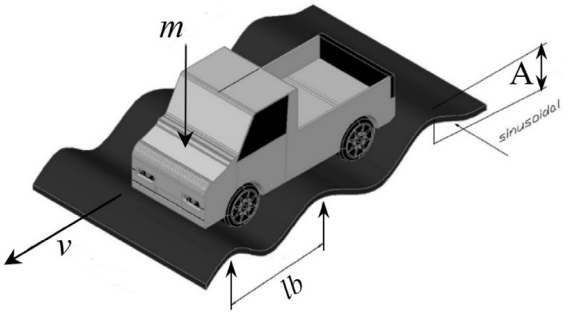

Fig. 1 Road profile

is based on a sinusoidal wavy pattern with road excitation height $A = 0.005$ m and road excitation wavelength $l_b = 0.3$ m.

The harmonic motion equation of the road profile, as the excitation source shown in Fig. 1, can be written as:

$$z_{\text{road}} = A\sin\left(\omega_{ext} t\right). \tag{2}$$

The variables in Eq. (2) are (A) the road profile amplitude height, ω_{ext} road profile excitation frequency, and t time.

2.2 Modeling of magnetorheological elastomer battery pack dampers

The design of the magnetorheological elastomer (MRE) battery pack damper is illustrated in Fig. 2, which is based on the Bouc Wen model developed for the damper system in an earthquake-resistant building featuring a sandwich model construction made up of 26 layers of MRE sheets with a 120 mm diameter and 1 mm thickness, alongside 25 steel sheets of the same dimensions (Yu et al., 2019). The steel sheets offer a load-bearing ability as an isolator in the vertical orientation, equating to a weight-bearing component for the structure. The performance of the base isolation system's vibration control is heavily reliant on the lateral stiffness of the device, which is calculated as $k = G_s . A/h_t$, where G_s is the shear elastic modulus of the MRE material, A is the cross-sectional area of the MRE layer, and h_t is the thickness of the MRE layer.

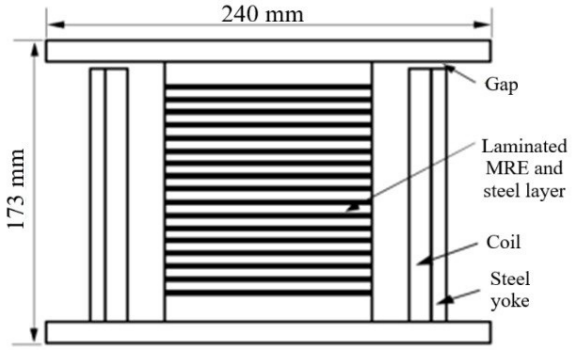

Fig. 2 Adaptive damper MRE (Yu et al., 2019)

Eq. (3) of the MRE mathematical model is based on the development of the Bouc Wen equation related to nonlinear quantities and the displacement force response hysteresis model (F), as follows (Leng et al., 2020):

$$F_{\text{MRE}} = k_0 x + c_0 \dot{x} + \alpha \cdot Z + F_0 . \tag{3}$$

The parameters c_0 and k_0 are the damping coefficient and stiffness of the MRE, respectively, which were obtained through experimental testing of the given magnetic field. F_0 is the force offset from the test by calculating the average value of the shear force in one MRE sampling cycle. The mathematical model of Eq. (3) describes the free body diagram shown in Fig. 3.

The intermediate variable Z in Bouc Wen's general equation represents a form of the hyperbolic hysteresis property model (Lin et al., 2023):

$$Z = \frac{1 - e^{-2\beta x}}{2e^{-\beta x}} . \tag{4}$$

The Bouc Wen's non-dimensional parameters α and β control the tendency of the strain-induced stiffness increase and adjust the shape (trim) of the hysteresis loop.

2.3 Optimization of MRE parameters using a genetic algorithm (GA)

The optimization strategies with GA to determine the previous MRE parameters that will be applied as a battery pack damper with vehicle speeds of 10, 20, and 30 km / h, which have sinusoidal road trajectories as in Eq. (2) comprises the following steps:

1. Formulation and Application of the Objective Function: The objective function $J(\Theta)$ is formulated based on the hysteresis model in Eq. (3), aiming to minimize the error between the experimental data

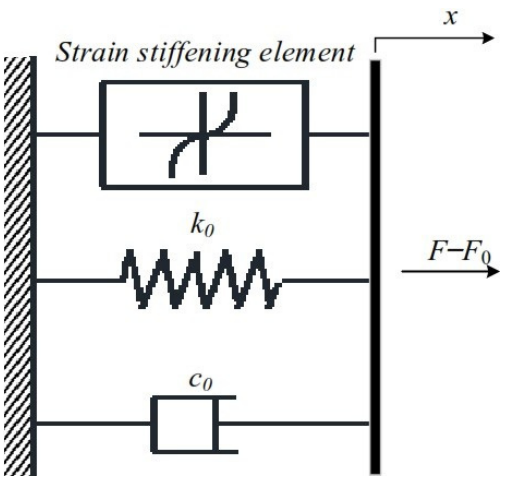

Fig. 3 Bouc wen modified (Yu et al., 2016)

and the model prediction. The Root Mean Square Error (RMSE) is used as the fitness metric:

$$J(\Theta) = \sqrt{\frac{1}{N}\sum_{i=1}^{N}\left[F_i^{\exp} - F_i^{\text{model}}(\Theta)\right]^2}, \quad (5)$$

where $\Theta = \{k_0, c_0, \alpha, \beta\}$ represents the set of parameters to be identified. F_i^{exp} is the experimental force measured at time step (i), $F_i^{\text{model}}(\Theta)$ is is the force predicted by the model (Eq. (16) for the front MRE or Eq. (17) for the rear MRE) at the i-th time step, using the experimental kinematic data (z_s, z_b, θ_b) and the parameter set Θ and N is the total number of data points in one sampling cycle.

2. Initialization of Algorithm Parameters and Population: The algorithm parameters were initialized to the number of populations $N_{pop} = 100$ and the maximum number of iterations $N_{it} = 500$. The upper and lower limits for each parameter were set to ±10% of the initial estimated values derived from experimental data (k_{exp}, c_{exp}, α_{exp}, β_{exp}) (Yu et al., 2016).
   - The stiffness and damping coefficient bounds:

     $k_0 \in [0.9\ k_{exp}, 1.1\ k_{exp}]$ and $c_0 \in [0.9\ c_{exp}, 1.1\ c_{exp}]$

   - The hysteresis parameters bounds:

     $\alpha \in [0.9\ \alpha_{exp}, 1.1\ \alpha_{exp}]$ and $\beta \in [0.9\ \beta_{exp}, 1.1\ \beta_{exp}]$

   An initial population of N_{pop} chromosomes is generated randomly within the defined search boundaries, where each chromosome represents a candidate solution $\Theta = [k_0, c_0, \alpha, \beta]$. The iteration counter is set to $t = 0$.
3. Fitness Evaluation: For each chromosome (candidate parameter set Θ) in the population, its fitness is calculated by evaluating the objective function $J(\Theta)$ defined in Eq. (5). This step quantifies how well each candidate solution performs.
4. The Genetic algorithm employed the following operators tailored for the continuous parameter optimization of the MRE model:
   - Selection: Tournament selection with size $k = 2$ was used to select parents based on their fitness values.
   - Crossover: Simulated Binary Crossover (SBX) with distribution index $\eta_c = 10$ and crossover probability $p_c = 0.8$ was applied to generate offspring by combining parent solutions.
   - Mutation: Polynomial mutation with distribution index $\eta_m = 20$ and mutation probability $p_m = 0.1$ per parameter was used to introduce diversity while maintaining solution feasibility within the established bounds (± 10% of initial estimated values).
5. Formation of New Population: The next-generation population ($t + 1$) was constructed by combining elite individuals from the current generation with the best offspring produced through selection, crossover, and mutation, ensuring the preservation of the best solution and monotonic optimization improvement.
6. Termination Criteria: The algorithm terminates when either the maximum number of generations ($N_{it} = 500$) is reached, or the improvement of the best fitness value falls below a predefined tolerance threshold ($1e^{-6}$) over 50 consecutive generations. Upon termination, the chromosome with the lowest fitness value (smallest RMSE) is selected as the optimal parameter set Θ_{optimal} for the MRE model.

Table 1 presents a comparison of the Bouc Wen parameter values obtained after optimization with the previous parameters of the MRE sample testing (Yu et al., 2016), conducted under conditions of a 4 Hz frequency and a 2 mm amplitude, with MRE magnetic generation utilizing currents of 1A and 2A.

The iteration process to find the optimal value of each MRE parameter *via* the genetic algorithm converged steadily at the best fitness value of the 1 and 2A MRE models at coordinates (224.265, 0.0501766) and (121.212, 0.0500057), as illustrated in Fig. 4.

The prototype semi-active battery pack damper design comprises a total size of 120 × 70 × 45 mm, as shown in Fig. 5. The magnetorheological elastomer specimen Fig. 5 (b) 40 × 25 × 10 mm is positioned at the center of the battery pack damper holder Fig. 5 (a), which also accommodates the AWG 18 coil Fig. 5 (c).

2.4 Dynamic modeling of the half-car 6 DOF

The free body diagram of the half-car model (6 DOF) for the Multipurpose Electric Vehicle (MPEV) and the four semi-active MRBDs mounted in the battery pack's corners below the chassis are shown in Fig. 6. Table 2 shows the parameters used in the dynamic modeling simulation.

The application of Newton's second law, along with D'Alembert's principle (refer to Eqs. (6), (9), (18), (20), and

Table 1 Comparison of the MRE parameters

Parameter MRE	Yu et al. (2016)		Optimized	
	1A	2A	1A*	2A*
k_0	16.382	21.093	18.02	22.096
c_0	0.648	1.063	0.713	1.063
α	3.795	31.803	4.174	33.916
β	1.227	0.640	1.350	0.648

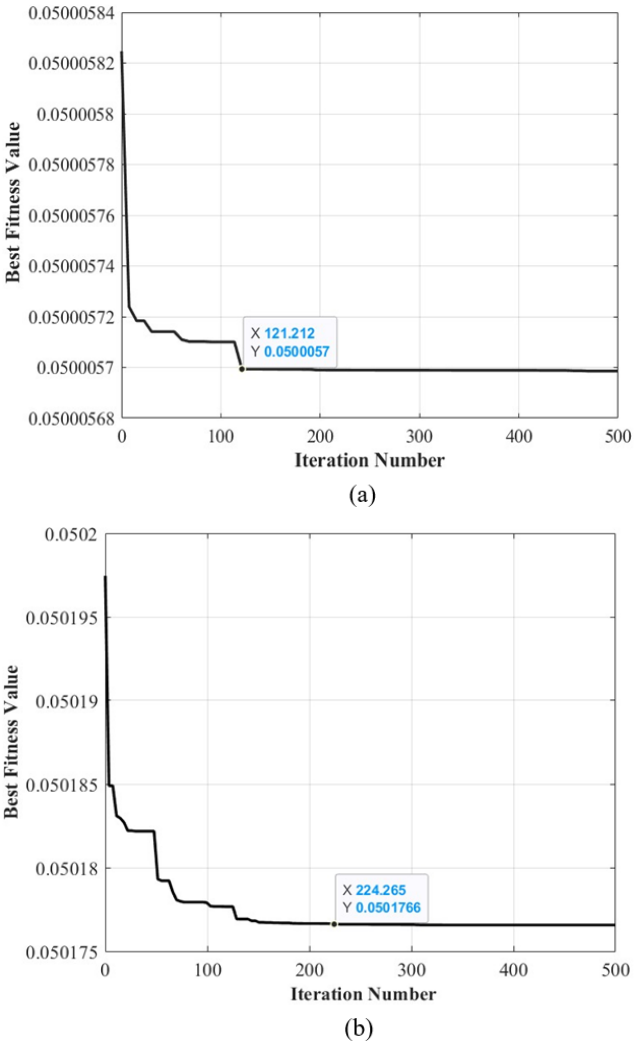

Fig. 4 Iteration process of parameters MRE by using GA: (a) 1A; (b) 2A

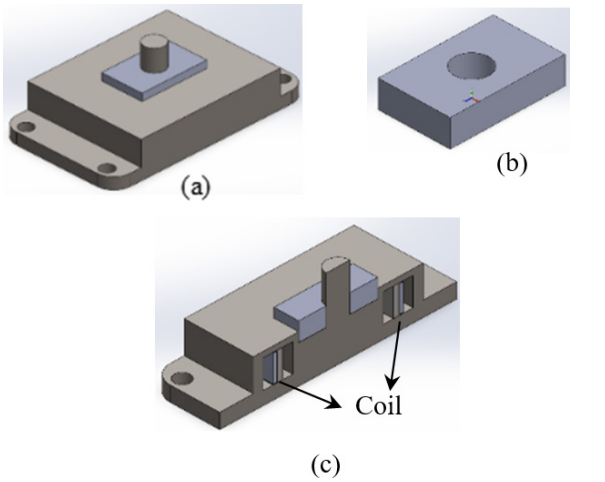

Fig. 5 Design Semi-Active MRE Battery Pack Damper (MRBD): (a) damper holder; (b) MRE pad; (c) Half-Section MRBD with Internal Coil

(22)), can be utilized to derive the equations of motion for both the unsprung and sprung masses in a 6-DOF half-vehicle dynamic model (Fig. 6) as follows:

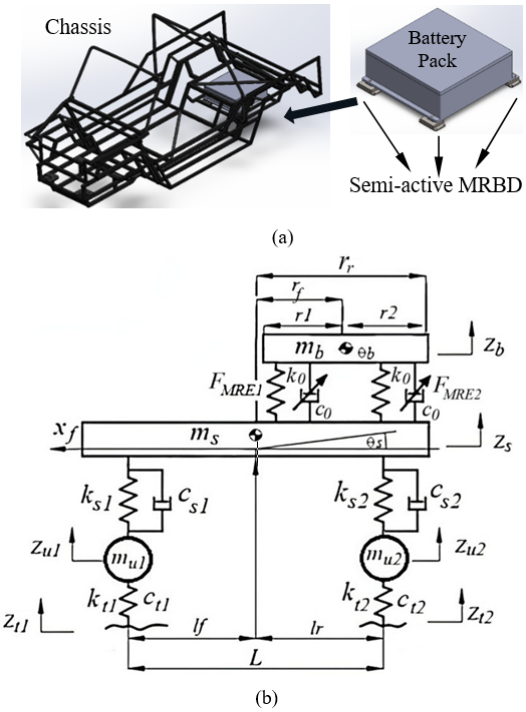

Fig. 6 (a) Located Semi-active MRBD and (b) Dynamic Model of a Half Car 6 DOF

Table 2 Vehicle parameters

Parameters	Symbol	Value
Chassis mass	m_s	850 kg
Front wheel mass	m_{u_1}	30 kg
Rear wheel mass	m_{u_2}	30 kg
Battery pack mass	m_b	200 kg
Distance chassis CG to front MRBD	r_f	0.887 m
Distance chassis CG to rear MRBD	r_r	1.392 m
Distance chassis CG to front wheel	l_f	1.13 m
Distance chassis CG to rear wheel	l_r	1.12 m
Distance battery pack CG front MRBD	r_1	0.265 m
Distance battery pack CG rear MRBD	r_2	0.265 m
Front suspension stiffness	k_{s_1}	16,000 N/m
Rear suspension stiffness	k_{s_2}	16,000 N/m
Front suspension damping	c_{s_1}	2,500 Ns/m
Rear suspension damping	c_{s_2}	1,500 Ns/m
Front tire stiffness	k_{t_1}	90,000N/m
Rear tire stiffness	k_{t_2}	160,000 N/m
Front tire damping	c_{t_1}	180 Ns/m
Rear tire damping	c_{t_2}	130 Ns/m
Front MRBD stiffness*	k_0	k_0 N/m
Rear MRBD stiffness*	k_0	k_0 N/m
Front MRBD damping*	c_0	c_0 Ns/m
Rear MRBD damping*	c_0	c_0 Ns/m
Chassis pitching angle	θ_s	rad
Battery pack pitching angle	θ_b	rad

* The values for the parameters k_0 and c_0 are derived from Table 1, which displays the results of the GA optimization.

1. Front wheel unsprung mass:

$$\sum F_{(t_1,s_1)} - m_{u_1} \cdot \ddot{Z}_{u_1} = 0\,, \tag{6}$$

$$F_{t_1} = -k_{t_1}\left(z_{t_1} - z_{u_1}\right) - c_{t_1}\left(\dot{z}_{t_1} - \dot{z}_{u_1}\right), \tag{7}$$

$$\begin{aligned} F_{s_1} &= k_{s_1}\left(z_{u_1} - \left(z_s - \left(l_f \cdot \theta_s\right)\right)\right) \\ &+ c_{s_1}\left(\dot{z}_{u_1} - \left(\dot{z}_s - \left(l_f \cdot \dot{\theta}_s\right)\right)\right) \end{aligned}. \tag{8}$$

2. Rear wheel unsprung mass:

$$\sum F_{(t_2,s_2)} - m_{u_2} \cdot \ddot{Z}_{u_2} = 0\,, \tag{9}$$

$$F_{t_2} = -k_{t_2}\left(z_{t_2} - z_{u_2}\right) - c_{t_2}\left(\dot{z}_{t_2} - \dot{z}_{u_2}\right), \tag{10}$$

$$\begin{aligned} F_{s_2} &= -k_{s_2}\left(z_{u_2} - \left(z_s - \left(l_r \cdot \theta_s\right)\right)\right) \\ &+ c_{s_2}\left(\dot{z}_{u_2} - \left(\dot{z}_s - \left(l_r \cdot \dot{\theta}_s\right)\right)\right) \end{aligned}. \tag{11}$$

The forces acting on the front and rear tires and suspension (unsprung mass) are F_{t_1} and F_{t_2}. Front and rear suspension forces are F_{s_1} and F_{s_2}. Displacement, wheel speed, suspension, and chassis affect wheel and suspension forces. The chassis pitching angle responses are θ_s and $\dot{\theta}_s$.

3. Vehicle chassis/body sprung mass:
The vehicle chassis is affected by forces on the front wheel suspension, rear wheel suspension, front and rear MRBD damper batteries:

$$\sum F_{(s1,s2,F_{\mathrm{MRE}_1},F_{\mathrm{MRE}_2})} - m_s \cdot \ddot{z}_s = 0\,, \tag{12}$$

$$m_s \ddot{z}_s = F_{s1} + F_{s2} - F_{\mathrm{MRE}_1} - F_{\mathrm{MRE}},\,. \tag{13}$$

A modified and expanded form of Bouc Wen's general equation was derived from the dynamic model depicted in Fig. 6, yielding the MRBD battery pack damper force equation as follows (Leng et al., 2020; Lin et al., 2023):

- Front (F_{MRE_1}) and Rear (F_{MRE_2}) MRBD forces:

$$\begin{aligned} F_{\mathrm{MRE}_1} &= k_0\left(z_s - \left(z_b - \left(r_1 \cdot \theta_b\right)\right)\right) \\ &+ c_0\left(\dot{z}_s - \left(\dot{z}_b - \left(r_1 \cdot \dot{\theta}_b\right)\right)\right) + \alpha \cdot Z_1 + F_0 \end{aligned}, \tag{14}$$

$$\begin{aligned} F_{\mathrm{MRE}_2} &= k_0\left(z_s - \left(z_b - \left(r_2 \cdot \theta b\right)\right)\right) + \\ & c_0\left(\dot{z}_s - \left(\dot{z}_b - \left(r_2 \cdot \dot{\theta} b\right)\right)\right) + \alpha \cdot Z_2 + F_0 \end{aligned}. \tag{15}$$

- Front (Z_1) and Rear (Z_2) MRE properties:

$$Z_1 = \frac{1 - e^{-2\beta\left(z_s - \left(z_b - \left(r_1 \cdot \theta_b\right)\right)\right)}}{2e^{-\beta\left(z_s - \left(z_b - \left(r_1 \cdot \theta_b\right)\right)\right)}} \tag{16}$$

$$Z_2 = \frac{1 - e^{-2\beta\left(z_s - \left(z_b - \left(r_2 \cdot \theta_b\right)\right)\right)}}{2e^{-\beta\left(z_s - \left(z_b - \left(r_2 \cdot \theta_b\right)\right)\right)}} \tag{17}$$

4. Battery pack sprung mass:
The battery pack sprung mass can be determined by summing Eqs. (10) and (11):

$$\sum F_{\left(F_{\mathrm{MRE}_1},F_{\mathrm{MRE}_2}\right)} - m_b \cdot \ddot{z}_b = 0\,, \tag{18}$$

$$m_b \ddot{z}_b = F_{\mathrm{MRE}_1} + F_{\mathrm{MRE}_2}\,. \tag{19}$$

5. Chassis pitching angle acceleration:

$$\sum \tau_{\text{chassis}} - I_S \cdot \ddot{\theta}_S = 0\,, \tag{20}$$

$$\begin{aligned} I_S \ddot{\theta}_S &= -l_f\left[F_{s_1}\right] + l_f\left[F_{s_2}\right] \\ &- r_f \cdot F_{\mathrm{MRE}_1} - r_r \cdot F_{\mathrm{MRE}_2} \end{aligned} \tag{21}$$

6. Battery pack pitching angle acceleration:

$$\sum \tau_{\text{battery pack}} - I_b \cdot \ddot{\theta}_b = 0\,, \tag{22}$$

$$I_b \ddot{\theta}_b = -r_1 \cdot F_{\mathrm{MRE}_1} - r_2 \cdot F_{\mathrm{MRE}_2}\,. \tag{23}$$

2.5 The 6 DOF frequency domain system

The process of extracting the frequency domain for a 6-DOF system necessitates the identification of the domains for matrices [***M***], [***C***], and [***K***] through the application of the eigenvalue method. More detailed matrices [***M***], [***C***], and [***K***] are presented in Appendix A.

The [F_{input}] consists of F_{u_1} and F_{u_2}, which were obtained by excitation of the road profile shape. From Eqs. (1) and (2), the excitation frequency ($f_t = \omega_{ext} / 2\pi$) will change with the vehicle speed (v) and wavelength (λ) as far as the distance x.

$$\begin{aligned} Z_{\text{road}}(x,t) &= A\sin\left(\frac{2\pi\ v\ t}{\lambda} + \omega_{ext} t\right) \\ &= A\sin\left(\frac{2\pi v}{\lambda} + \omega_{ext}\right) t \end{aligned} \tag{24}$$

The excitation frequency due to the moving vehicle is called the effective excitation frequency (ω_{eff}), which is equal to ($2\pi v + \lambda\ \omega_{ext}$) so that Eq. (24) becomes:

$$Z_{\text{road}}(x,t) = A\sin\left[\left(2\pi v + \omega_{eff}\lambda\right)_t\right]. \tag{25}$$

The displacement and acceleration response of the front wheel (z_{u1})t, with a distance from the axis to the rear wheel (z_{u2})t of $L = l_f + l_r$, is given by:

$$Z_{u_1}(t) = A\sin\left(\omega_{eff} \cdot t\right), \tag{26}$$

$$Z_{u_2}(t) = A\sin\left(\omega_{eff} \cdot t - \frac{2\pi L}{\lambda}\right), \tag{27}$$

$$\dot{Z}_{u_1}(t) = A\omega_{eff}\cos\left(\omega_{eff} \cdot t\right), \tag{28}$$

$$\dot{Z}_{u_2}(t) = A\omega_{eff}\cos\left(\omega_{eff} \cdot t - \frac{2\pi L}{\lambda}\right). \tag{29}$$

The rotational responses of the chassis (θ_s) and battery pack (θ_b) are influenced by the moment of inertia and can be expressed as follows:

$$\theta_s(t) = \iint \ddot{\theta}_s dt^2 . \tag{30}$$

The mode shape ($\boldsymbol{Z}$) in Eq. (31) is determined by the eigenvector of a 6 degree of freedom MRBD:

$$\boldsymbol{Z} = \begin{Bmatrix} Z_s \\ Z_{u_1} \\ Z_{u_2} \\ \theta_s \\ \theta_b \\ Z_b \end{Bmatrix}. \tag{31}$$

Eq. (28) shows the force input matrices [F_{input}] for the front wheel (F_{u_1}) and rear wheel (F_{u_2}), which are determined by the wheel stiffness and damping coefficients, which are linked to the displacement and acceleration, as outlined in Eqs. (26) to (29).

$$\begin{aligned} F_{u_1} &= k_{t_1}\left[z_{t_1} - A\sin\left(\omega_{eff}\cdot t\right)\right] \\ &+ c_{t_1}\left[\dot{z}_{t_1} - A\omega_{eff}\cos\left(\omega_{eff}\cdot t\right)\right], \end{aligned} \tag{32}$$

$$\begin{aligned} F_{u_2} &= k_{t_2}\left[z_{t_2} - A\sin\left(\omega_{eff}\cdot t - \frac{2\pi L}{\lambda}\right)\right] \\ &+ c_{t_2}\left[\dot{z}_{t_2} - A\omega_{eff}\cos\left(\omega_{eff}\cdot t - \frac{2\pi L}{\lambda}\right)\right]. \end{aligned} \tag{33}$$

$$F_{\text{input}} = \begin{bmatrix} 0 \\ F_{u_1} \\ F_{u_2} \\ 0 \\ 0 \\ 0 \end{bmatrix}. \tag{34}$$

The matrices were analyzed numerically to calculate the natural frequency and the damping ratio in relation to the source of the excitation frequency. The natural frequency can be determined by numerically calculating the eigenvalues between the stiffness matrix $\boldsymbol{K}$ and the mass matrix $\boldsymbol{M}$:

$$\left([\boldsymbol{K}] - \lambda_{eig}[\boldsymbol{M}]\right)\boldsymbol{Z} = 0 \ , \ \left([\boldsymbol{C}], \left[F_{\text{input}}\right]\right) = 0 \cdot$$

The natural frequency (ω_n) of each mode in the 6-DOF system is determined as follows:

$$\left|\omega_n\right|_i = \sqrt{\lambda_{eig_i}} . \tag{35}$$

The numerical equation employed to calculate the damping coefficient matrix $\boldsymbol{C}$ in each mode of the 6-DOF system, incorporating all damping elements from the front and rear wheels, as well as the front and rear MRBD and suspensions, is as follows:

$$\zeta_i = \frac{[\boldsymbol{C}]}{2\sqrt{[\boldsymbol{K}][\boldsymbol{M}]}} . \tag{36}$$

The MRBD's capability to maintain the battery pack's stability is achieved by reducing the vibration transfer through a transmissibility spectrum of the battery pack displacement (z_b) and the vibration source input from the front wheel and rear wheel (z_{u_1} and z_{u_2}), utilizing the Laplace transformation ($s = j\omega_{eff}$) as described in Eq. (37), which is then converted to the frequency domain so the battery pack's transmissibility function becomes:

$$\left(-\omega_{eff}^2 M + j\omega_{eff} C + K\right)\boldsymbol{Z}\left(\omega_{eff}\right) = F_{input}\left(\omega_{eff}\right). \tag{37}$$

The $H(\omega_{eff})$ transfer function relates the response $z_b(\omega_{eff})$ to the input load $F_{\text{input}}(\omega_{eff})$:

$$H\left(\omega_{eff}\right) = \left(-\omega_{eff}^2 M + j\omega_{eff} C + K\right)^{-1} . \tag{38}$$

The response z_b is determined using the dynamic model system structure of $H(\omega_{eff})$, which involves extracting the element vector $\boldsymbol{Z}\left(\omega_{eff}\right)$, equivalent to:

$$\begin{aligned} &\left[Z_s, Z_{u_1}, Z_{u_2}, \theta_s, \theta_b, z_b\right]^T , \\ &Z_b\left(\omega_{eff}\right) = H_{6,1}\left(\omega_{eff}\right)F_{u_1} + H_{6,2}\left(\omega_{eff}\right)F_{u_2} . \end{aligned} \tag{39}$$

The transmissibility equation of $T_b(\omega_{eff})$ describes the relationship between the amplitude response ratio $z_b(\omega_{eff})$ and the effect of converting the input excitation force into corresponding amplitude responses in the front and rear wheels (z_{u_1} and z_{u_2}):

$$T_b\left(\omega_{eff}\right) = \frac{\left|z_b\left(\omega_{eff}\right)\right|}{\sqrt{\left|z_{u_1}\left(\omega_{eff}\right)\right|^2 + \left|z_{u_2}\left(\omega_{eff}\right)\right|^2}} . \tag{40}$$

2.6 Semi-active controller design

In this study, a semi-active control system was developed for the MRE damper, serving as a support and vibration isolator for both the front and rear battery packs. This system is controlled based on the MRBD 1A and MRBD 2A electric currents, utilizing the $F_c = F_{\text{MRE}_1} + F_{\text{MRE}_2}$ force control algorithm.

The developed sliding surface ensures system convergence and yields the desired response. This work presents a straightforward sliding surface based on a single scalar parameter, $\lambda_{ss} > 0$. The sliding surface, S MRBD is defined as:

$$S = \dot{z}_b + \lambda_{ss} z_b . \tag{41}$$

Assuming $r_1 = r_2$, then the dynamic equation of the battery pack Eq. (19) adopts an active isolator:

$$\ddot{z}_b = \rho_b F_c + \vartheta\phi + g_b \,, \tag{42}$$

where ρ_b, ϑ, and ϕ are, respectively, the scalar factor of the control input parameter, the vector parameter, and the state vector regressor of the system:

$$\rho_b = \frac{1}{m_b},\ \vartheta = \frac{1}{m_b},\ \begin{bmatrix} -2c_0 \\ c_0(r_1 - r_2) \\ -2k_0 \\ k_0(r_1 - r_2) \end{bmatrix}^T \quad \phi = \begin{bmatrix} \dot{z}_b \\ \dot{\theta}_b \\ z_b \\ \theta_b \end{bmatrix}.$$

The chassis signals are quantified, namely the component associated with the excitation from the chassis (g_b). Let Γ_b be a known component that satisfies the following conditions:

$$g_b = -2c_0\dot{z}_s - 2k_0 z_s, |g_b|_{\max} \le \Gamma_b \,. \tag{43}$$

The dynamics system is reformulated in sliding surface terms for MRBD:

$$\dot{S} = \rho_b F_c + \vartheta\phi + \lambda_{ss}\dot{z}_b + g_b \,. \tag{44}$$

The uncertainty in the model parameters ρ_b and ϑ can be denoted by the estimated values $\hat{\rho}_b$ and $\hat{\vartheta}$, which are associated with the estimated errors $\tilde{\rho}_b = \hat{\rho}_b - \rho_b$ and $\tilde{\vartheta} = \hat{\vartheta} - \vartheta$, respectively. The optimal representation of the active actuator force F_c is as follows:

$$F_c = -\left(\hat{\rho}_b\right)^{-1}\left[\mathbb{k}S + \vartheta\phi + \lambda_{ss}\dot{Z}_b + \Gamma_b \mathrm{sign}(S)\right]. \tag{45}$$

Therefore, the proposed adaptive algorithm:

$$\dot{\hat{\rho}}_b = \sigma_{b_1}\frac{1}{\hat{\rho}_b}S\left[\mathbb{k}S + \vartheta\phi + \lambda_{ss}\dot{Z}_b + \Gamma_b \mathrm{sign}(S)\right], \tag{46}$$

$$\dot{\hat{\vartheta}} = \sigma_{b_2}S\phi \,, \tag{47}$$

where the gains $\mathbb{k}$, $\sigma_{b,1}$ and $\sigma_{b,2}$ are positive constants of the adaptive control algorithm, the closed-loop system in Eq. (44) ensures convergence and vibration damping if the following two conditions are satisfied:

1. $\phi(t) \to 0$ as $t \to \infty$.
2. All signals must be bounded for $\forall t \ge 0$.

MRE dampers are semi-active, therefore their force response F_{MRE} ($F_{\mathrm{MRE_1}}$ at the front and $F_{\mathrm{MRE_2}}$ at the rear) cannot always match an active control law's optimum control force F_c. For MRE devices, the sole control input is coil current (I), not force. A clippedoptimal two-stage technique is used:

1. An ideal active controller calculates the desired force F_c.
2. The MRE force tracks this target without breaking passivity as a passive on–off controller sets the current.

The adaptive controller's output to current clipped on–off rule is:

$$I = I_{\max} H\left(\left(F_c - F_{\mathrm{MRE}_{1,2}}\right)F_{\mathrm{MRE}_{1,2}}\right). \tag{48}$$

The control current for the MRE damper is denoted by I in Eq. (48), the Heaviside function is represented by H, and the maximum current value applied to attain maximum stiffness is denoted by $I_{\max} = 2A$. Furthermore, the force measured at the base isolator MRE is denoted by $F_{\mathrm{MRE}_{1,2}}$, while the optimum control force value is F_c, as determined by Eq. (45). $F_{\mathrm{MRE}_{1,2}}$ are computed in the simulation using Model (Yu et al., 2016). According to Eq. (48), the control algorithm is divided into two phases:

$$I = \begin{cases} I_{\max} & \text{if}\left(F_c - F_{\mathrm{MRE}_{1,2}}\right)F_{\mathrm{MRE}_{1,2}} > 0 \\ 0 & \text{if}\left(F_c - F_{\mathrm{MRE}_{1,2}}\right)F_{\mathrm{MRE}_{1,2}} \le 0 \end{cases}. \tag{49}$$

3 Results and discussion

3.1 Characteristics model of the MRE hysteresis

The parameter in Table 1 is based on the shape of the hysteresis model, which has a constant non-linearity when looping according to the rules of the strain stiffening phenomenon through the results of testing the MRE specimens of force against displacement with activation currents of 1A and 2A, amplitude of 2 mm at an excitation frequency of 4 Hz.

Fig. 7 illustrates the comparison between two magnetorheological elastomer hysteresis loop graphs obtained from the experiments performed by Yu et al. (2019) and the outcomes of parameter optimization achieved through the use of the GA objective function, as defined by Eq. (5). MRE model was assessed in a dynamic test to evaluate the dynamic characteristics of the MRE, one of which was conducted at a displacement amplitude of 2 mm and a frequency of 4 Hz with a magnetic field induction current applied on MRE 1A and 2A (Yu et al., 2016). The Bouc Wen model exhibits viscoelastic properties that are capable of handling shear loads under supply currents ranging from 1A to 3A. The deformation changes in Fig. 7 (a) and 7 (b) depict the behavior of the MRE of the Bouc Wen model, which exhibits unique characteristics in strain stiffening. The force shift observed in Yang Yu's MRE model, as depicted in Fig. 7 (b), shows a larger displacement during the loading and unloading processes when using a 2A magnetic field generator compared to a 1A MRE. The forces derived from the loading and unloading of the parameters k, c, α, and β, which were optimized from the objective function equation, exceeded those seen in experiments conducted by previous studies (Yu et al., 2019). A comparison of the area under the hysterical curve of the optimization results using

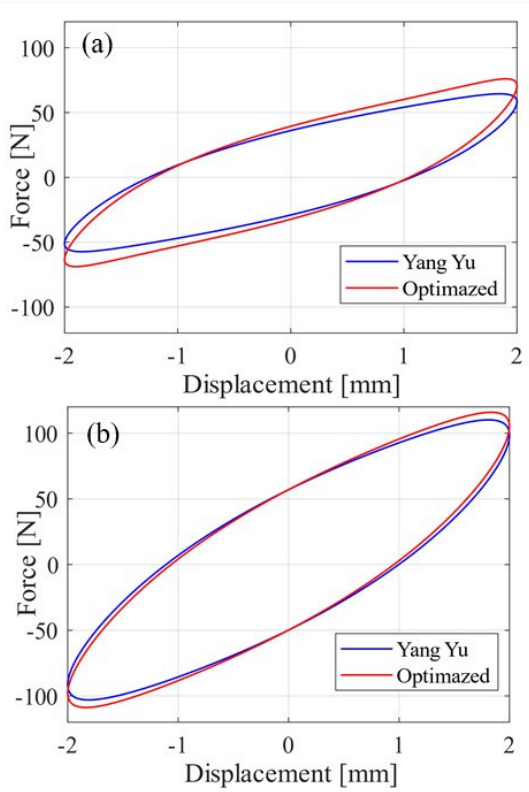

Fig. 7 Comparison of the Loop Hyteresis Response of Yu et al., (2019) and the Optimized MRE specimens: (a) 1A; (b) 2A

the trapezoidal numerical method showed that the values in Table 3 were greater before optimization for both 1A and 2A.

The magnitude of the load and the area of the hysteresis loop in the MRE are affected by the quantity of current supplied to the system during the magnetic field induction. The generation of magnetic field affects the stiffness of the MRE, which will increase until it reaches the MRE material stress saturation point where the maximum shear modulus cannot handle the applied load. The effectiveness of the MRE parameters k_0, c_0, α, β (Table 1) increases with increasing loading current (I) and exhibits a nearly linear correlation with a first-order polynomial function, as stated by (Yu et al., 2019; Yu et al., 2016):

$$k_{eff} = k_0 + I \cdot k_{\exp}, \tag{50}$$

$$c_{eff} = c_0 + I \cdot c_{\exp}, \tag{51}$$

Table 3 Comparison of optimized hysteresis loop parameters with the Yu et al., (2019) MRE Model

Model MRE	Displacement [mm] ($Disp_{min}$, $Disp_{max}$)	Force [N] (F_{min}, F_{max})	Hysteresis Loop Area [mm^2]
Yu et al., (2019) 1A	(−2,2)	(−63.25, 64.43)	2,045.28
Optimization 1A	(−2,2)	(−74.5, 75.97)	2,249.90
Yu et al., (2019) 2A	(−2,2)	(−109.1, 110.16)	3,356.38
Optimization 2A	(−2,2)	(−114.5, 115.92)	3,357.77

$$\alpha_{eff} = \alpha + I \cdot \alpha_{\exp}, \tag{52}$$

$$\beta_{eff} = \beta + I \cdot \beta_{\exp}. \tag{53}$$

3.2 Dynamic displacement responses

The performance of the MRBD semi-active isolator model installed on top of the vehicle chassis is evaluated in Fig. 6. A comparative study was conducted by comparing the simulation of the dynamic response of the battery pack with variations in vehicle speed on a sinusoidal road field between those using MRBD and those without MRBD (WOMRBD). The dynamic response of the battery pack without the MRBD (i.e., the battery is placed and bolted on the rear chassis) is shown in Fig. 6. To ensure that the MRBD simulation on the battery pack works in accordance with the dynamic model equations, the determination of the excitation frequency range based on the provisions of ISO 8606:2016 standard is 1.39 Hz (10 km/h), 2.78 Hz (20 km/h) and 4.17 Hz (30 km/h) with an amplitude of 0.035 m.

Fig. 8 shows the simulation of the time series dynamic response graph compared to the displacement of the battery pack without (WOMRBD) or using the optimized MRE isolator damper MRBD 1A (pink) and 2A (green) with vehicle speeds variations of 10 km/h (Fig. 8 (a)), 20 km/h (Fig. 8 (b)) and 30 km/h (Fig. 8 (c)). From the results in Fig. 8, it is very clear that the difference when the vehicle passes the sinusoidal road topography, the simulation of the battery pack without WOMRBD under 2 s, at all speed variations produces the highest displacement and is unstable or shackling on the battery pack. However, after 2 s, the shaking is absent and the vibration tends to stabilize. The vibration density of the battery pack without MRBD is more intense per second but has a decrease in displacement with increasing vehicle speed. On the other hand, battery packs that use optimized MRE isolator dampers (MRBD) at both 1A and 2A have a drastic decrease in displacement oscillation movements at each peak to peak reaching 94.88%. Furthermore, the displacement response oscillations of the battery packs show that MRBD 1A and 2A have the opposite direction to WOMRBD, indicating that the MRE battery pack damping system works in a different direction from the oscillation direction as a response to balance the direction of movement.

3.3 Acceleration dynamic responses

The simulation results illustrating the acceleration response of the battery pack MRBD 1A, MRBD 2A, and the scenario without the MRE damper (WOMRBD) under vehicle speed variations of 10, 20, and 30 km/h are presented in Fig. 9. The MRBD 1A and 2A damper isolation systems not only reduce the acceleration response but also manage

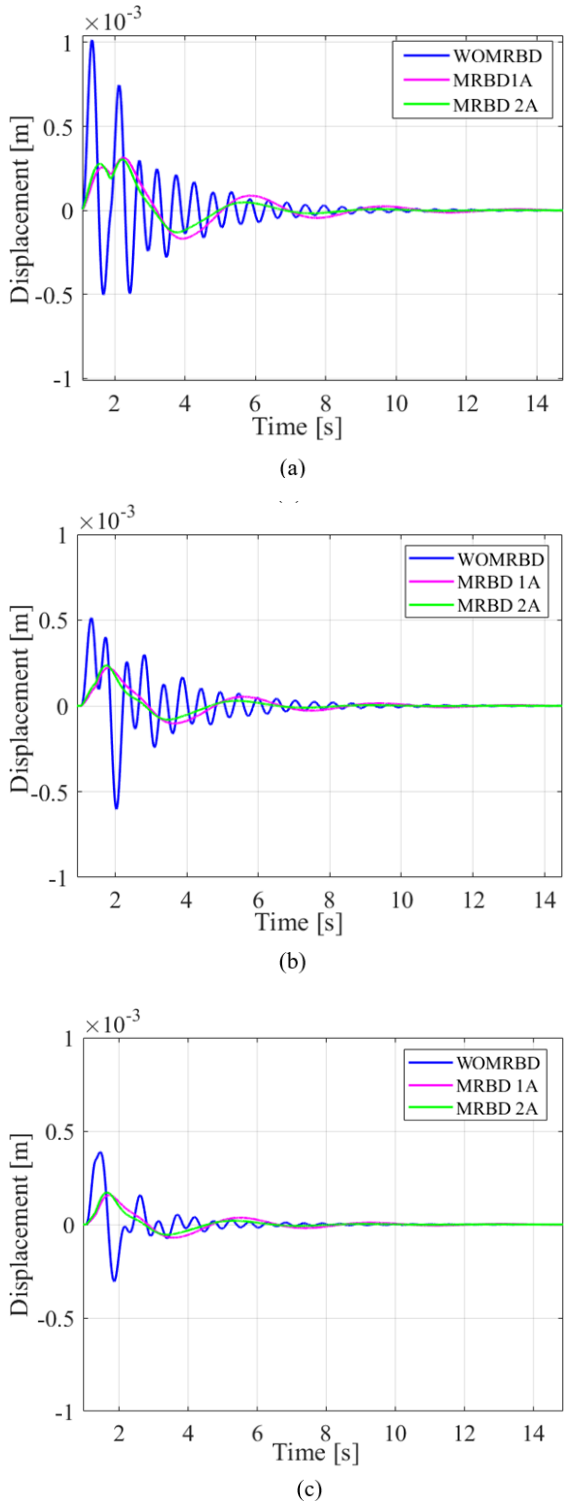

Fig. 8 Dynamic response for displacement at various speeds: (a) 10 km/h; (b) 20 km/h; (c) 30 km/h

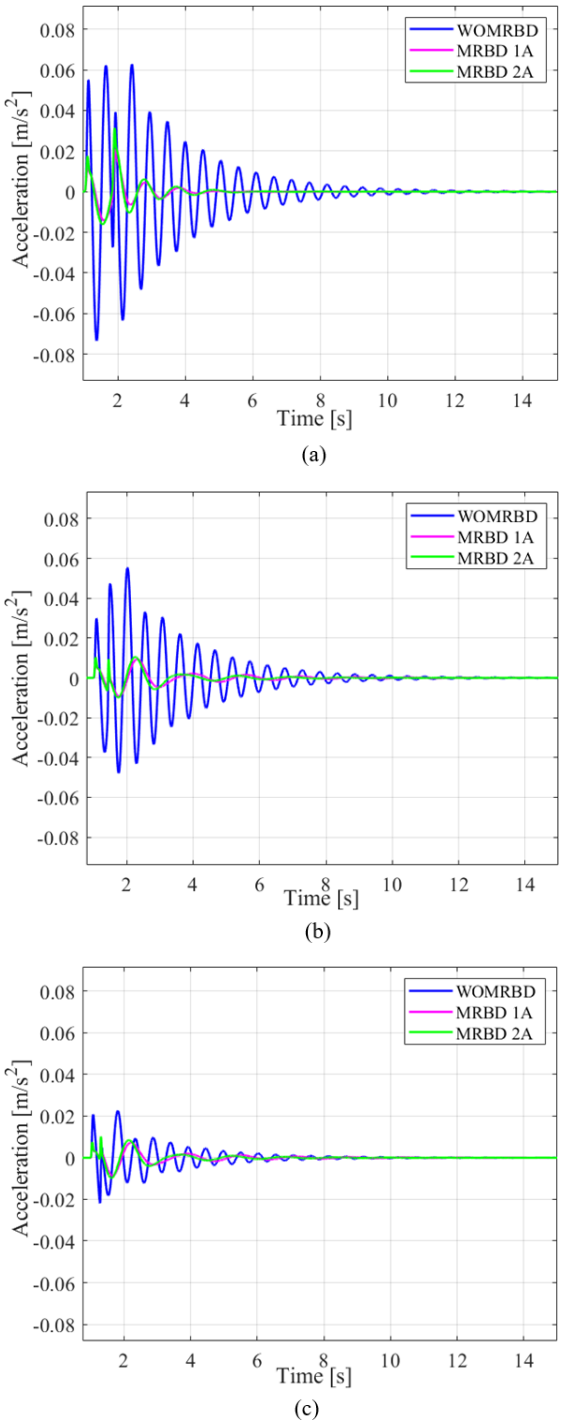

Fig. 9 Dynamic response for acceleration at various speeds: (a) 10 km/h; (b) 20 km/h; (c) 30 km/h

to keep the battery pack's acceleration at a relatively lower magnitude during the vehicle's excitation period compared to a battery pack without MRE, such as the one denoted as WOMRBD. The acceleration response is a sign of the vibration transmission experienced by the battery pack as the vehicle travels over a road profile excited by a sinusoidal motion. At vehicle speeds of 10, 20, and 30 km/h, the response and acceleration density of the battery pack without the MRE (WOMRBD) increased from peak to peak. The acceleration response value starts to decline until it reaches a stable level at 12 s. In contrast, the simulation of the application of MRBD 1A and 2A dampers to the battery pack successfully reduced the acceleration response

resulting from the sinusoidal excitation of the road profile across all tested vehicle speeds of 10, 20, and 30 km/h.

The declining acceleration response is affected by the stiffness and damping characteristics of the MRE produced by the magnetic field. The goal of optimizing the MRE parameters was to enhance the vibration isolation, and this improvement is evident from the considerable reduction in the acceleration response. The acceleration response of the MRBD 2A battery pack exhibits stable values of 0.014 m/s^2 at vehicle speeds of 10 km/h and 20 km/h, which are comparable to one another. In contrast, the MRBD 1A battery pack yielded lower acceleration responses, specifically 0.002 m/s^2 and 0.01 m/s^2 lower than MRBD 2A. At a speed of 30 km/h, MRBD variants 1A and 2A exhibited the lowest acceleration response stability, with values of 0.001 m/s^2 and 0.003 m/s^2, respectively.

3.4 Damping force characteristics

The characteristics of the damping force in relation to the velocity response of the MRBD battery pack damper, which is installed in a vehicle traveling at speeds of 10, 20, and 30 km/h, are illustrated in Fig. 10, where it is evident that the damping force exhibits non-linear behavior. In general, the MRBD 1A and 2A mounted on the battery pack damper system exhibited a greater behavior of the damping force at all vehicle speed variations compared to the system without the damper. The battery pack without a damper (WOMRBD) exhibits linear characteristics, resulting in no damping, and consequently, the vibration effect of the chassis response (z_s) is directly transmitted to the battery pack. The damping force F_d in the MRBD damper comprises the linear relationship between the damping constant and the velocity response, as well as the non-linear interaction of the MRE hysteresis parameter, specifically the effective loop shape control parameter (α_{eff}) and the exponential saturation phase parameter (β_{eff}) as described by Eq. (54):

$$F_d = c_{eff} \cdot \left[\dot{z}_b\right] + \alpha_{eff} \cdot \mathrm{sgn}\left[\dot{z}_b\right] \cdot \left(1 - e^{-\beta \cdot |\dot{z}_b|}\right). \quad (54)$$

The battery pack velocity response, denoted as , is the derivative of the acceleration response given in Eq. (19).

The dynamic response of the MRBD includes the interaction between the excitation forces from the front and rear wheel responses that are transmitted to the spring system and the vehicle chassis at speeds of 10, 20, and 30 km/h crossing the sinusoidal road surface and forwarded to the MRBD damper system so that the vibration effect toward the battery pack will be anticipated by the effect of MRBD magnetic field generation. The changing vehicle speed affects the damping force received by the battery pack. The magnetic field generated by the electric current flowing through the coil in the MRBD damper will modulate the properties of the magnetorheological elastomer, resulting in a controlled change in the damping parameter ceff to the amount of damping force

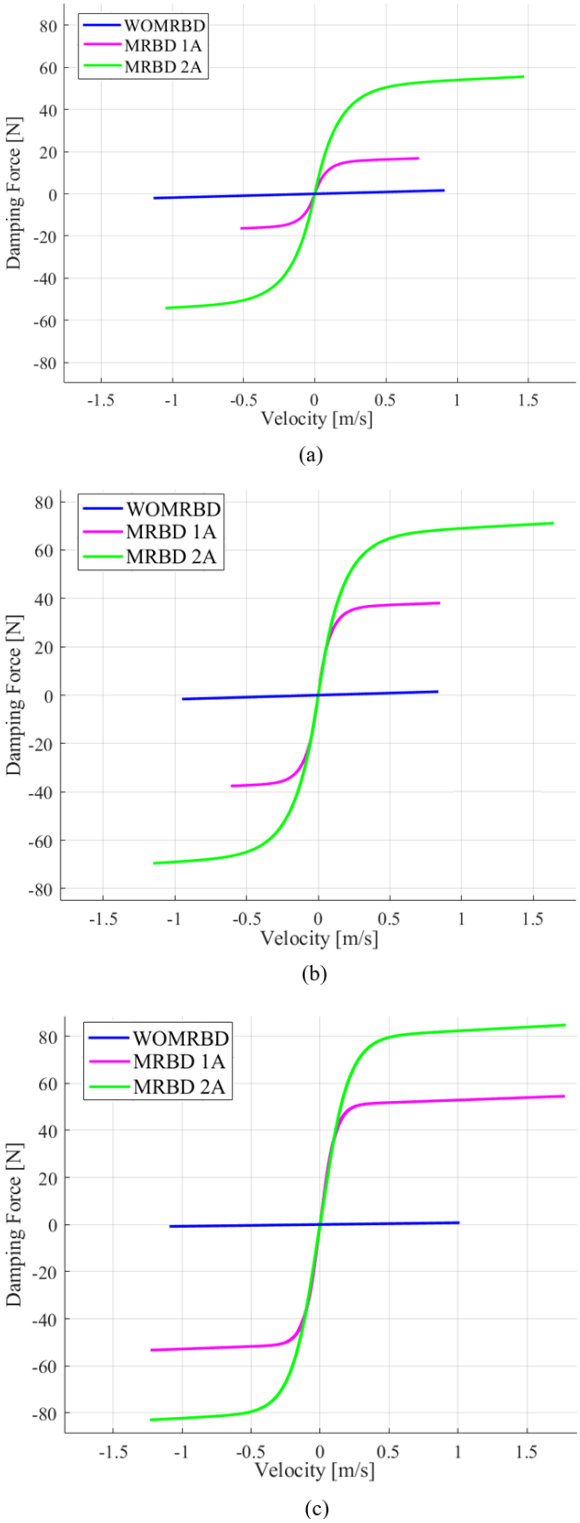

Fig. 10 Damping force at various speeds:
(a) 10 km/h; (b) 20 km/h; (c) 30 km/h

in real-time. By increasing ceff, the system will be more responsive to the vertical movement speed and more efficient in reducing bounce and maintaining stability. In this case, the generation of magnetic fields with currents of 1 and 2 A can dynamically change the properties of the elastomer against changes in the magnitude of the damping force, which will affect the stability response of the battery pack.

A distinct hysteresis pattern is evident in Fig. 10 (c) at speeds of 30 km/h for the MRBD 2A configuration, unlike the MRBD 1A configuration, which shows an increasing gap between the onset of non-linear effects during both the restoring and compressing phases, in comparison to speeds of 10 km/h and 20 km/h. At lower speeds, a vehicle traveling at 30 km/h encounters a more considerable amping force before reaching its peak damping force, despite experiencing a quicker speed response time. The α and β non-linearity parameters influence the parameters that control the slope, steepness, and point of saturation of the damping force within the hysteresis loop. The elastic properties of the MRE damper material have a substantial effect on the loading process, especially during the restoration and compression stages, in order to attain the highest level of damping force generation before the system transitions to a nonlinear state and reaches its saturation point.

A comparison of the maximum restore and maximum compress damping force values for the battery pack, using the MRBD 1A, MRBD 2A dampers, and without the damper (WOMRBD), is illustrated in Table 4, at various vehicle speeds. The battery pack without a damper (WOMRBD) yielded linear and small variations in the slope of the ramps on the damping force, as revealed by both Fig. 10 and Table 4 in the process of cyclic restoration and compression. The battery pack's vibration absorption is lower without the damper than with the damper because the damping force is directly related to the velocity response. The slopes of MRBD 1A and MRBD 2A exhibit a greater inclination than that of WOMRBD at every velocity response during both the restoration phase, where the velocity is greater than 0 ($v > 0$), and the compression phase, where the velocity is less than 0 ($v < 0$), indicating the impact of the damping constant Fig. 10 (c) when paired with a magnetic field driven by a current of 1 and 2A.

In the restoration and compression phases, the damping force magnitude was equal in both, but with opposing directions, reaching peaks of 54.4 N and −52.43 N at a vehicle speed of 30 km/h in MRBD 2A. The coordinates adjacent to MRBD 1A are 36.16° N and −31.19° N. Vehicle speeds of 10 and 20 km/h have lower maximum damping forces.

3.5 Power spectral density

The simulation of the battery packs with and without MRE is shown in Fig. 11, which considers the power distribution intensity in the frequency domain at vehicle speeds of 10, 20, and 30 km/h. These speeds exhibit the same trend, with the PSD value initially increasing up to 1 Hz before decreasing, ultimately resulting in vibration fluctuations. The PSD value increases substantially until it reaches its peak at the Peak Point, after which it decreases intermittently until it reaches a frequency of 50 Hz.

The comparisons show that the peak value of the PSD curve without the MRE (WOMRBD) is higher at lower working frequencies than the peak value of the curve with MRBD. The power transferred to the battery pack *via* vibration, without damper (WOMRBD), was greater at all vehicle speeds compared with the MRBD 1A and 2A cases. The battery pack with MRBD 1A and 2A specifications has the capability to absorb or reduce the vibration energy caused by the road profile excitation. Furthermore, the introduction of a magnetic field will enhance the stiffness and damping characteristics of the MRE, as well as decrease the vibration energy, with the associated energy dissipation (E_{dis}) being increased, as indicated by the relationship described in Eq. (55):

$$E_{dis} = \int_0^t c_{eff} \cdot \left[\dot{z}_b(t)\right]^2 dt \,. \tag{55}$$

The vibration damping system, in addition to the dissipating energy, encompasses the total energy calculated *via* a numerical integration of Fig. 11, utilizing the trapezoid method applied to Eq. (56) of the PSD frequency spectrum data $S_x(f)$:

$$E_{\text{total}} = \int_{f\max}^{f\max} S_x(f)\, df \,. \tag{56}$$

Table 4 Damping forces at various speed

Variation	10 km/h		20 km/h		30 km/h	
	Velocity $\left(F_{d_{\text{restore}}}\right)$	Velocity $\left(F_{d_{\text{compress}}}\right)$	Velocity $\left(F_{d_{\text{restore}}}\right)$	Velocity $\left(F_{d_{\text{compress}}}\right)$	Velocity $\left(F_{d_{\text{restore}}}\right)$	Velocity $\left(F_{d_{\text{compress}}}\right)$
WOMRBD	(0.91, 2.36)	(−1.14, −1.63)	(0.93, 1.79)	(−1.07, −1.19)	(1.08, 1.01)	(−1.19, −0.34)
MRBD 1A	(0.04, 8.89)	(−0.05, −4.54)	(0.07, 22.08)	(−0.08, −21.29)	(0.10, 36.16)	(−0.10, −31.19)
MRBDt 2A	(0.08, 21.59)	(−0.08, −20.14)	(0.15, 38.48)	(−0.14, −35.57)	(0.18, 54.40)	(−0.18, −52.13)

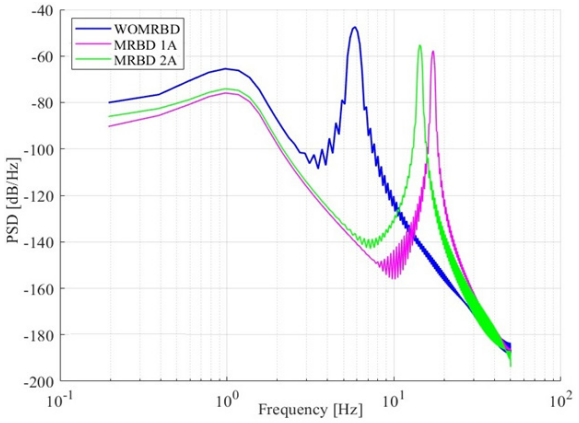

(a)

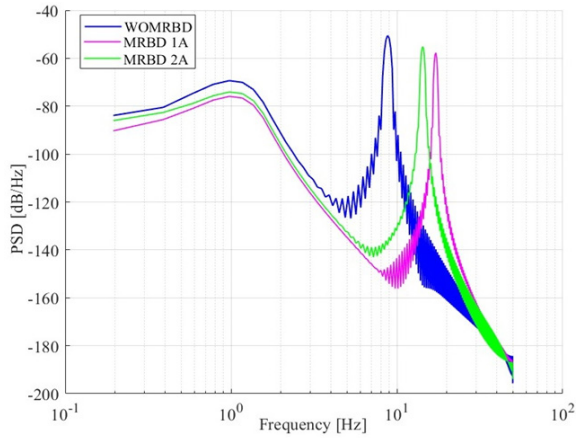

(b)

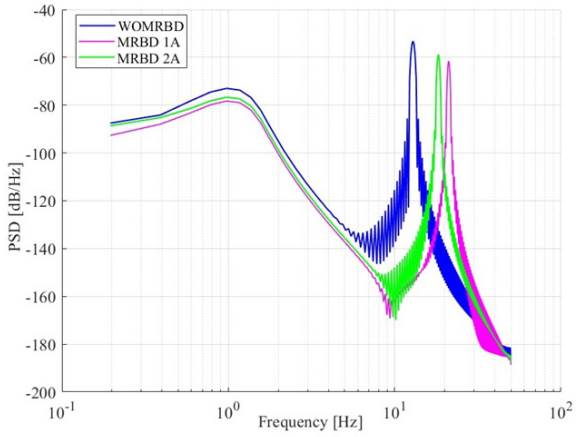

(c)

Fig. 11 Distribution power density of the battery pack at various speeds: (a) 10 km/h; (b) 20 km/h; (c) 30 km/h

The effectiveness of MRBD 1A and MRBD 2A in reducing vibration can be evaluated by examining the amount of vibration energy (E_{trans}) transmitted to the battery pack, which is the difference between the energy dissipated and the total energy absorbed by the damper, as illustrated by Eq. (57):

$$E_{\text{trans}} = E_{\text{total}} - E_{dis} \,. \tag{57}$$

A comparison of the energy balance is presented in Table 5, focusing on the battery pack without the MRE (WOMRBD) in conjunction with MRBD 1A and 2A. The highest vibration energy transferred to the MRDB 1A and MRDB 2A battery packs were 51.4% and 39.3%, respectively, as shown in Table 5, when the speed was 20 km/h.

3.6 Transmissibility responses

To enhance the analysis of the battery pack's MRE damper on the vibration spectral power density, as presented in Fig. 10, it is essential to assess the transmissibility of the battery pack with the MRBD damper. According to Eq. (34), the battery pack's transmissibility amplitude response magnitude is affected by the displacement of both the front and rear wheels within the excitation frequency domain.

A comparison of the amplitude-to-frequency transmissibility properties of the dynamic response of the battery pack with and without the MRBD is shown in Fig. 12 at vehicle speeds of 10, 20, and 30 km/h, in relation to a sinusoidal road profile with six degrees of freedom, as per the dynamic model presented in Fig. 6. The battery pack without the MRE (WOMRBD) showed a transmissibility response pattern characterized by numerous distinct peaks of maximum transmissibility at particular frequencies.

The difference in the peak transmissibility value is linked to the natural frequency of the battery system without the MRE (WOMRBD), which is used as a reference point in planning the implementation of the MRE dampers. The transmissibility graphs of the battery packs incorporating MRBD 1A and MRBD 2A dampers had lower peaks and were not aligned with the battery's natural frequency, suggesting that the MRBD dampers effectively isolate vibrations from resonating frequencies.

Table 6 provides the peak point information for each transmissibility graph in Fig. 12, organized by the 10, 20, and 30 km/h variations in vehicle speed. The excitation frequency grouping was performed in accordance with the SAE J2380 standard, covering a range of low frequencies from 0.1 to 10 Hz, as well as medium frequencies spanning 10 to 50 Hz. Peak transmissibility is typically not observed across various vehicle speeds at low frequency for MRBD 2A. The results demonstrate the influence of the MRE stiffness and damping parameters, which were determined through optimization simulations using a 2A magnetic field flow, and are capable of enhancing the vibration damping as a result of the road surface profiles. The use of MRBD dampers can substantially decrease the amplitude of the resonance. The transmissibility amplitude value is seen at the medium frequency

Table 5 Peak Energy dissipation and total energy comparison

Variation	10 km/h		20 km/h		30 km/h	
	$E_{dis} = S_{X\max}$ [dB/Hz]*	E_{tot} [KW/Hz]	$E_{dis} = S_{X\max}$ [dB/Hz]*	E_{tot} [KW/Hz]	$E_{dis} = S_{X\max}$ [dB/Hz]*	E_{tot} [KW/Hz]
WOMRBD	−47.45 @ 5.85 Hz	0.0109	−51.55@8.98 Hz	0.00532	−53.17@12.89 Hz	0.00285
MRBD 1A	−57.75 @17.19 Hz	0.00102	−57.75@17.19 Hz	0.00102	−61.54@21.09 Hz	0.000426
MRBD 2A	−55.65 @14.45 Hz	0.00186	−55.65@14.45 Hz	0.00186	−58.85@18.36 Hz	0.000784

* 1PSD (Watt/Hz) = $10^{\frac{\mathrm{PSD}(dB/Hz)}{10}}$

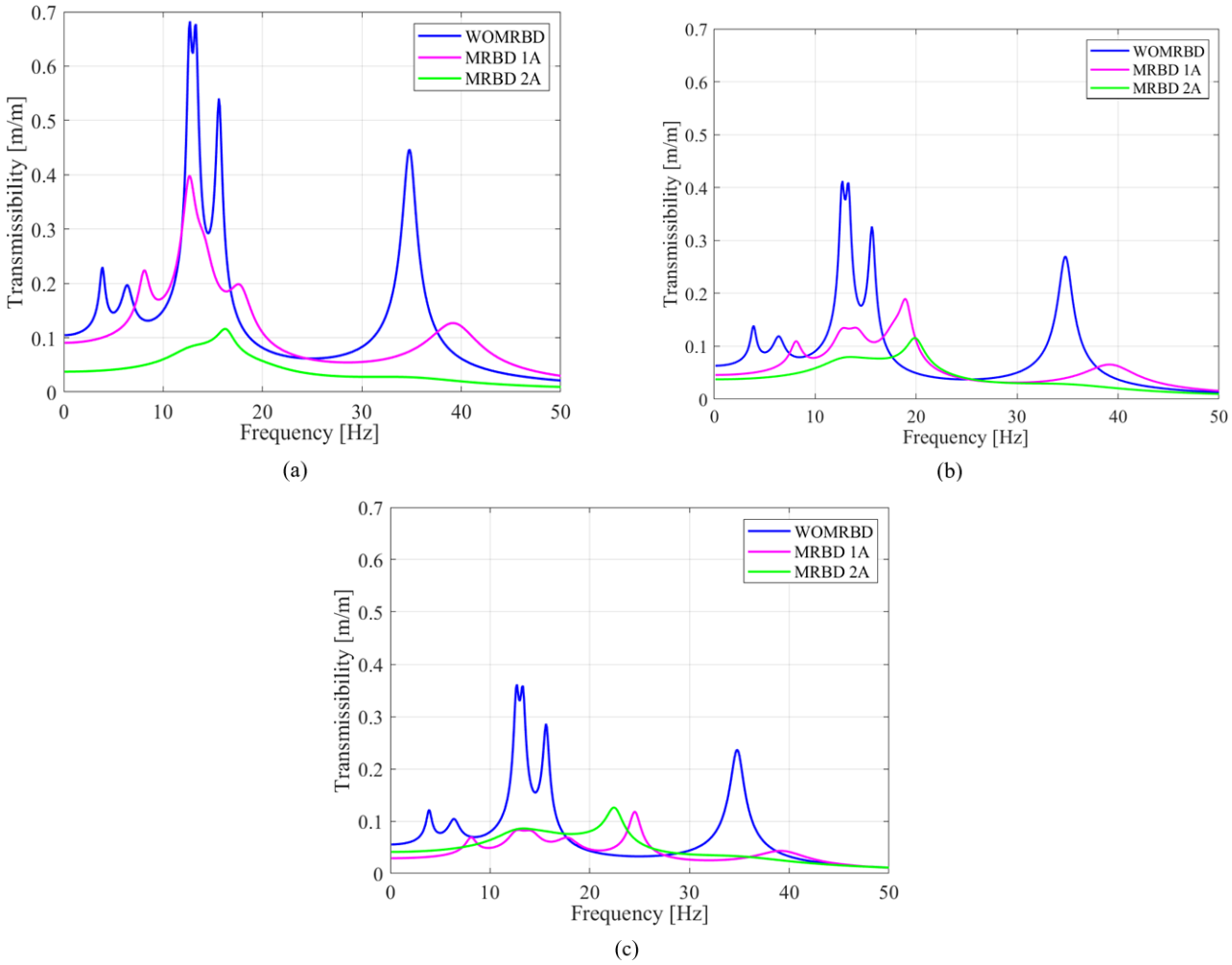

Fig. 12 Characteristics of the battery pack transmissibility at various speeds (a) 10 km/h, (b) 20 km/h and (c) 30 km/h

of 12.7 Hz in the case of a battery pack using MRBD 1A and without MRE (WOMRBD), for vehicle speeds of 10 km/h corresponding to 0.682 and 0.398, respectively. The highest rate of transmission of MRBD 2A occurred at a vehicle speed of 30 km/h within the medium frequency range of 22.4 Hz at 0.126. In contrast, the simulation results from MRBD 1A for the battery pack suggest the possibility of increasing the resonance amplitude, since it shares the same natural frequency of 12.7 Hz as WOMRBD, as depicted in Fig. 12 (a) and referenced in Table 6 within the low-frequency range which is highlighted in yellow.

4 Conclusion

The first phase of this study focuses on the development of MRE applications in the design of prototype battery pack vibration dampers by simulating MRE parameters through GA optimization to predict the dynamic response, damping force distribution, power spectral density and transmissibility function mechanism for each working frequency to reduce the resonance effects in the electric vehicle battery pack system. The simulation results show that semi-active MRBD 1A and 2A worked effectively compared to WOMRBD which covers several aspects including:

Table 6 Peak natural frequency and transmissibility comparison

Vehicle speeds	ISO 8606* ω_{ext}	Peak WOMRBD		Peak MRBD 1A		Peak MRBD 2A	
		$T(\omega_{eff})$	ω_n (Hz)	$T(\omega_{eff})$	ω_n (Hz)	$T(\omega_{eff})$	ω_n (Hz)
10 km/h**	0.1–10 Hz Low frequency	0.229	3.9				
		0.196	6.4	0.224	8.1		
		0.682	12.7	0.398	12.7		
	10–50 Hz Medium frequency	0.677	13.3				
		0.540	15.6	0.199	17.6	0.116	16.3
		0.446	34.8	0.127	39.3		
20 km/h	0.1–10 Hz Low frequency	0.139	3.9				
		0.199	6.4	0.109	8.1		
		0.412	12.7	0.134	12.9		
	10–50 Hz Medium frequency	0.409	13.3	0.135	13.9	0.079	13.6
		0.326	15.6	0.189	18.9	0.116	19.9
		0.269	34.8	0.065	39.2		
30 km/h	0.1–10 Hz Low frequency	0.122	3.9				
		0.104	6.4	0.069	8.1		
		0.361	12.7	0.083	12.9		
	10–50 Hz Medium frequency	0.359	13.3	0.082	13.9	0.086	13.4
		0.286	15.6	0.069	17.7		
				0.117	24.6	0.126	22.4
		0.236	34.8	0.043	39.1		

*) International Organization for Standardization (ISO), (2016)
**) Yellow-highlighted values represent medium-frequency resonance at 10 km/h (ω_n = 12.7 Hz)

1. The optimization of the Bouc-Wen model MRE damper *via* the genetic algorithm (GA) best fitting method yields new MRE parameters k_0, c_0, α, β which can optimize the load restoration and compression hysteresis loop process to reduce the dynamic response of displacement and acceleration across all vehicle speed variations when traversing sinusoidal road profiles, thus minimizing the effect of front and rear wheel bounce and enhancing the stability of the battery pack's position and amplitude response.
2. The MRBD 1A and MRBD 2A systems exhibit a substantial damping slope during phase restoration and phase compression due to the creation of 1 and 2A magnetic fields and the nonlinear effects of the MRE's hysteresis loops, specifically α_{eff} and β_{eff}, until the MRE damper reaches saturation, at which point the damping constant c_{eff} is unable to match the increase in the speed response.
3. The MRBD 1A and MRBD 2A prototype designs exhibit a lower energy density spectrum distribution per unit frequency compared to the WOMRBD, signifying a reduction in intense fluctuations within the low and medium frequency range, which in turn results in increased dissipation energy to absorb vibration energy, thus preventing it from being transmitted to the battery pack.
4. The resonance effect is only observed in MRBD 1A at low frequencies, occurring at a speed of 10 km/h relative to the base peak of WOMRBD. In most cases, the highest transmissibility levels in MRBD 1A and MRBD 2A across all vehicle speed and excitation frequency variations are lower than those in WOMRBD, except for a peak transmissibility that could lead to resonance at 10 km/h in the low frequency range for MRBD 1A when compared with WOMRBD, necessitating further simulation using vibration distribution related 3D numerical models.
5. A numerical simulation served as the foundation for the development and testing of the prototype battery pack dampers for electric vehicles.

Acknowledgment
This work was supported by the Ministry of Education, Culture, Research, and Technology of the Republic of Indonesia, which provided funding from The Indonesian

Education Scholarship Program (BPI) through collaborative efforts from the Center for Higher Education Funding (BPPT) and The Indonesia Endowment Funds for Education (LPDP) in 2024.

References

Abdillah, M. F., Budiman, B. A., Prasetio, I. P., Sambegoro, P. L. (2021) "Minimizing Dynamic Loading Resonance of Battery Pack Subjected to Road Profile Loads", IOP Conference Series: Materials Science and Engineering, 1109(1), 012012. https://doi.org/10.1088/1757-899X/1109/1/012012

Belingardi, G., Scattina, A. (2023) "Battery Pack and Underbody: Integration in the Structure Design for Battery Electric Vehicles—Challenges and Solutions", Vehicles, 5(2), pp. 498–514. https://doi.org/10.3390/vehicles5020028

Galvagno, E., Vigliani, A., Velardocchia, M. (2018) "Transient response and frequency domain analysis of an electrically variable transmission", Advances in Mechanical Engineering, 10(5), 1687814018776182. https://doi.org/10.1177/1687814018776182

Hári, L. R. (2022) "Spectral Non-Stationarity in Road Vehicle Vibrations", Periodica Polytechnica Transportation Engineering, 51(1), pp. 79–88. https://doi.org/10.3311/PPtr.18318

Heinzen, T., Plaumann, B., Kaatz, M. (2023) "Influences on Vibration Load Testing Levels for BEV Automotive Battery Packs", Vehicles, 5(2), pp. 446–463. https://doi.org/10.3390/vehicles5020025

Hua, X., Thomas, A. (2021) "Effect of dynamic loads and vibrations on lithium-ion batteries", Journal of Low Frequency Noise, Vibration and Active Control, 40(4), pp. 1927–1934. https://doi.org/10.1177/14613484211008112

ISO (2016) "ISO 8606:2016, Mechanical vibration – Road surface profiles – Reporting of measured data", International Organization for Standardization, Genf, Switzerland.

Khairi, M. H. A., Garik, L. J., Mazlan, S. A., Mohd Yusuf, S. Y., Johari, M. A. F., Nordin, N. A., Imaduddin, F. (2024) "Tensile Properties of Isotropic and Anisotropic Magnetorheological Elastomer With and Without Magnetic Field Application", International Journal of Automotive Mechanical Engineering, 21(1), pp. 11036–11044. https://doi.org/10.15282/ijame.21.1.2024.07.0853

Ladipo, I. L., Fadly, J. D., Faris, W. F. (2016) "Characterization of Magnetorheological Elastomer (MRE) Engine Mounts", materials today: Proceedings, 3(2), pp. 411–418. https://doi.org/10.1016/j.matpr.2016.01.029

Leng, D., Sun, S., Xu, K., Liu, G. (2020) "A physical model of magnetorheological elastomer isolator and its dynamic analysis", Journal of Intelligent Material Systems and Structures, 31(9), pp. 1141–1156. https://doi.org/10.1177/1045389X20910272

Lin, D., Yang, F., Gong, D., Li, R. (2023) "A new vibration isolator integrating tunable stiffness-damping and active driving properties based on radial-chains magnetorheological elastomer", Mechanical Systems and Signal Processing, 183, 109633. https://doi.org/10.1016/j.ymssp.2022.109633

Liu, C., Hemmatian, M., Sedaghati, R., Wen, G. (2020) "Development and Control of Magnetorheological Elastomer-Based Semi-active Seat Suspension Isolator Using Adaptive Neural Network", Frontiers in Materials, 7, 171. https://doi.org/10.3389/fmats.2020.00171

Nguyen, V., Le, V., Jiao, R., Yuan, H. (2020) "Low-frequency vibration analysis of heavy vehicle suspension system under various operating conditions", Mathematical Models in Engineering, 6(1), pp. 13–22. https://doi.org/10.21595/mme.2019.21229

Prażnowski, K., Mamala, J. (2016) "Classification of the road surface condition on the basis of vibrations of the sprung mass in a passenger car", IOP Conference Series: Materials Science and Engineering, 148, 012022. https://doi.org/10.1088/1757-899X/148/1/012022

Priyandoko, G., Suwandono, P., Ubaidillah, U. (2021) "Development of vibration isolator using magnetorheological elastomer", Journal of Applied Engineering Science 19(4), pp. 1108–1113. https://doi.org/10.5937/jaes0-28945

Ramalingam, M., Thirumurugan, M. A., Kumar, T. A., Jebaseelan, D. D., Jebaraj, C. (2020) "Response characteristics of car seat suspension using intelligent control policies under small and large bump excitations", International Journal of Dynamics and Control, 8(2), pp. 545–557. https://doi.org/10.1007/s40435-019-00569-y

SAE International Recommended Practice "Vibration Testing of Electric Vehicle Batteries, SAE Standard J2380_201312", SAE International, Warrendale PA, USA, 2013. https://doi.org/10.4271/J2380_201312

Shui, L., Chen, F., Garg, A., Peng, X., Bao, N., Zhang, J. (2018) "Design optimization of battery pack enclosure for electric vehicle", Structural and Multidisciplinary Optimization, 58(1), pp. 331–347. https://doi.org/10.1007/s00158-018-1901-y

Sobri, N. S., Hudha, K., Kadir, Z. A., Amer, N. H., Ahmad, K. Z. K., Rahmat, M. S. (2024) "Parameter optimization of anisotropic polarization in magnetorheological elastomers for enhanced impact absorption capability using the Taguchi method", Journal of the Mechanical Behavior of Materials, 33(1), 20240003. https://doi.org/10.1515/jmbm-2024-0003

Susatio, Y., Oktaviana, L., Rizki, N. K., Listijorini, E., Biyanto, T. R. (2018) "Design of half-car active suspension system for passenger riding comfort", Journal of Physics: Conference Series, 1075(1), 012030. https://doi.org/10.1088/1742-6596/1075/1/012030

Székely, P., Ficzere, P. (2017) "The Examination of Dynamic Effects of Shape Optimized Vehicle Components", Periodica Polytechnica Transportation Engineering, 45(2), pp. 90–93. https://doi.org/10.3311/PPtr.9875

Tang, L., Ren, N. L., Funkhouser, S. (2023) "Semi-active Suspension Control with PSO Tuned LQR Controller Based on MR Damper", International Journal of Automotive and Mechanical Engineering, 20(2), pp. 10512–10522. https://doi.org/10.15282/ijame.20.2.2023.13.0811

Unuh, M. H., Muhamad, P., Yakub, F., Ismail, M. A., Tanasta, Z. (2019) "Experimental Validation to a Prototype Magnetorheological (MR) Semi-Active Damper for C-Class Vehicle", International Journal of Automotive and Mechanical Engineering, 16(3), pp. 7034–7047. https://doi.org/10.15282/ijame.16.3.2019.15.0527

Venczel, M., Veress, Á., Peredy, Z. (2022) "Past and Future Practical Solutions for Torsional Vibration Damping in Vehicle Industry", Periodica Polytechnica Transportation Engineering, 50(4), pp. 318–329. https://doi.org/10.3311/PPtr.19194

Yang, Z., Lee, S., Lee, K., Velayudham, V. (2022) "Random Vibration Analysis for a Battery Enclosure of Electric Vehicle", presented at 2022 WCX SAE World Congress Experience, Detroit, Mich, Apr. 5–7. https://doi.org/10.4271/2022-01-0705

Yu, Y., Li, J., Li, Y., Li, S., Li, H., Wang, W. (2019) "Comparative Investigation of Phenomenological Modeling for Hysteresis Responses of Magnetorheological Elastomer Devices", International Journal of Molecular Sciences, 20(13), 3216. https://doi.org/10.3390/ijms20133216

Yu, Y., Royel, S., Li, J., Li, Y., Ha, Q. (2016) "Magnetorheological elastomer base isolator for earthquake response mitigation on building structures: modeling and second-order sliding mode control", Earthquakes and Structures, 11(6), pp. 943–966. https://doi.org/10.12989/EAS.2016.11.6.943

Yudianto, A., Kurniadi, N., Wayan Adiyasa, I., Arifin, Z. (2019) "The Effect of Masses in the Determination of Optimal Suspension Damping Coefficient", Journal of Physics: Conference Series, 1273(1), 012067. https://doi.org/10.1088/1742-6596/1273/1/012067

Zainordin, A. Z., Mohamed, Z. (2024) "Performance Characteristics of a Compact Core Annular-Radial Magnetorheological Damper for Vehicle Suspension Systems", International Journal of Automotive and Mechanical Engineering, 21(4), pp. 11757–11769. https://doi.org/10.15282/ijame.21.4.2024.3.0906

Zhao, B., Nagayama, T. (2017) "IRI Estimation by the Frequency Domain Analysis of Vehicle Dynamic Responses", Procedia Engineering, 188, pp. 9–16. https://doi.org/10.1016/j.proeng.2017.04.451

Zhu, H., Yang, J., Zhang, Y. (2018) "Modeling and optimization for pneumatically pitch-interconnected suspensions of a vehicle", Journal of Sound and Vibration, 432, pp. 290–309. https://doi.org/10.1016/j.jsv.2018.06.043

Appendix A

Matrix [*M*]

Matrix ***M*** is the mass matrix of the 6-DOF half-car system, representing the inertia properties of the vehicle components. It consists of the equivalent masses of the unsprung masses (m_{u_1} , m_{u_2}), the sprung mass (m_s), and the rotational inertias associated with the pitch motion of the sprung mass (I_s) and the battery pack system (I_b).

$$[\boldsymbol{M}] = \begin{bmatrix} m_{u_1} & 0 & 0 & 0 & 0 & 0 \\ 0 & m_{u_2} & 0 & 0 & 0 & 0 \\ 0 & 0 & m_s & 0 & 0 & 0 \\ 0 & 0 & 0 & m_b & 0 & 0 \\ 0 & 0 & 0 & 0 & I_s & 0 \\ 0 & 0 & 0 & 0 & 0 & I_b \end{bmatrix}$$

Matrix [*C*]

Matrix ***C*** is the damping matrix of the 6-DOF system, representing the energy dissipation mechanisms arising from the suspension damping and the magnetorheological battery damper (MRBD) installed at the chassis–battery pack interface. It incorporates the front and rear suspension damping coefficients (c_{s_1} , c_{s_2}), the corresponding tire damping coefficients (c_{t_1} , c_{t_2}), and the controllable damping contribution of the MRBD (c_0), thereby governing the vibration attenuation behavior of the system in the frequency domain.

$$[\boldsymbol{C}] = \begin{bmatrix} c_{t_1}+c_{s_1} & 0 & -c_{s_1} & 0 & c_{s_1}l_f & 0 \\ 0 & c_{t_2}+c_{s_2} & -c_{s_2} & 0 & c_{s_2}l_r & 0 \\ c_{s_1} & c_{s_2} & -c_{s_1}-c_{s_2}-2_{c_0} & 2c_0 & c_{s_1}l_f + c_{s_2}l_r - c_0(r_1+r_2) & 0 \\ 0 & 0 & 2_{c_0} & -2c_0 & c_0(r_1+r_2) & 0 \\ -c_{s_1}l_f & c_{s_2}l_r & c_{s_1}l_f - c_{s_2}l_r - c_0(r_1+r_2) & c_0(r_1+r_2) & -c_{s_1}l_f^2 + c_{s_2}l_r^2 - c_0(r_1^2+r_2^2) & 0 \\ 0 & 0 & 0 & 0 & 0 & 0 \end{bmatrix}$$

Matrix [*K*]

Matrix ***K*** defines the elastic stiffness properties of the system, including the front and rear tire stiffness (k_{t_1} , k_{t_2}), the suspension stiffness (k_{s_1} , k_{s_2}), and the controllable stiffness contribution of the MRBD (k_0). This matrix governs the restoring forces acting on the system and is essential for determining the natural frequencies and mode shapes of the 6-DOF model.

$$[\boldsymbol{K}] = \begin{bmatrix} k_{t_1}+k_{s_1} & 0 & -k_{s_1} & 0 & k_{s_1}l_f & 0 \\ 0 & k_{t_2}+k_{s_2} & -k_{s_2} & 0 & k_{s_2}l_r & 0 \\ k_{s_1} & k_{s_2} & -k_{s_1}-k_{s_2}-2k_0 & 2k_0 & k_{s_1}l_f + k_{s_2}l_r - k_0(r_1+r_2) & 0 \\ 0 & 0 & 2k_0 & -2k_0 & 0 & 0 \\ -k_{s_1}l_f & k_{s_2}\cdot l_r & k_{s_1}l_f - k_{s_2}l_r - k_0(r_1+r_2) & k_0(r_1+r_2) & -k_{s_1}l_f^2 + k_{s_2}l_r^2 - k_0(r_1^2+r_2^2) & 0 \\ 0 & 0 & 0 & 0 & 0 & 0 \end{bmatrix}$$